

An electro-optical bunch profile monitor for FCC-ee

M. Reissig,* E. Bründermann, S. Funkner, L.L. Grimm, B. Härer, G. Niehues, J. L. Steinmann, and A.-S. Müller
Karlsruhe Institute of Technology (KIT), 76131 Karlsruhe, Germany

R. Corsini, A. Gilardi, S. Mazzoni,[†] C. Pakuza, A. Schloegelhofer, and T. Lefevre
CERN, 1211 Geneva 23, Switzerland

P. Korysko
University of Oxford, Oxford, England and
CERN, 1211 Geneva 23, Switzerland
(Dated: October 3, 2025)

The Future Circular Lepton Collider (FCC-ee) presents challenges for a longitudinal bunch profile monitor due to its wide range of bunch lengths and charge densities across its four distinct operational modes. For commissioning, monitoring the top-up injection, and energy calibration, the FCC-ee requires non-destructive, single-shot measurements of the bunch length and profile. This contribution proposes an in-vacuum electro-optical (EO) longitudinal bunch profile monitor for single-shot measurements at high repetition rates, building on the successful EO monitor at the Karlsruhe Research Accelerator (KARA) at the Karlsruhe Institute of Technology. A novel single-pass conceptual design for the in-vacuum holder of the electro-optical crystal is presented, utilizing prisms instead of a mirror to guide the laser through the crystal, which additionally allows measurements of the long bunches foreseen for FCC-ee operation mode at the Z-pole energy. A first prototype has been constructed and tested at the in-air test stand of the CERN Linear Electron Accelerator for Research (CLEAR). Results from the prototype tests are presented, demonstrating the proof of principle for the single-pass prism-based EO monitor design for FCC-ee.

I. INTRODUCTION

The future circular electron-positron collider (FCC-ee) is planned to be a precision instrument with highest luminosity to study Z, W, Higgs, and top particles at the smallest scales [1]. The FCC innovation study (FCCIS) evaluates the feasibility of this project in great detail including civil engineering considerations, beam optics, design of the accelerating RF cavities and beam guiding magnets as well as beam instrumentation for the commissioning and operation of the machine [2], resulting in the recently published feasibility report [3, 4]. Within this project, this contribution summarizes the study of an electro-optical (EO) bunch profile monitor for FCC-ee, including a first prototype test.

This bunch profile monitor needs to perform single-shot measurements of high-intensity, picosecond-long particle bunches with the bunch length data available in a timescale of minutes while still maintaining a sub-picosecond resolution [1, p. 426]. A typically used streak camera for determining the length of optical pulses is challenging here, as a very extensive optical beamline would have to be designed due to the large dipole bending radius of ~ 9.9 km [5]. Another candidate for longitudinal beam instrumentation is the usage of Cherenkov diffraction radiation in a dielectric material, which is a newer technique for non-invasive bunch length measurements and is also under investigation for FCC-ee [6].

This contribution focuses on an EO setup, which makes use of the Pockels effect in EO crystals to probe the Coulomb field of the particle bunches with laser pulses. This principle was successfully used in an electro-optical spectral decoding (EOSD) setup for single-shot bunch profile measurements with sub-picosecond resolution at linear accelerators [7–9]. The EOSD setup can also be adapted to circular accelerators, which pose a challenge due to the MHz-revolution frequencies and wakefield-induced heating, as proven for the first time by the Karlsruhe Research Accelerator (KARA) at the Karlsruhe Institute of Technology [10, 11]. Its implementation of EOSD for single-shot and turn-by-turn bunch profile measurements enables revealing the dynamics of the ultra-relativistic electron bunches in a non-equilibrium state [12]. This setup serves as a baseline for the development of an EO bunch profile monitor for FCC-ee, where unprecedented beam parameters introduce new challenges for the monitor design.

II. ELECTRO-OPTICAL TECHNIQUES

The EOSD principle is depicted in Fig. 1, which starts with a chirped laser pulse that is sent into the vacuum chamber and propagates through an EO crystal in parallel to the electron beam. In this first step, the birefringence of the crystal is modulated by the Coulomb field of the passing electron bunch due to the Pockels effect. This results in a polarization modulation of the incident laser pulse while traveling through the crystal. In the following step, the polarization modulation is translated to an

* micha.reissig@kit.edu

[†] Deceased.

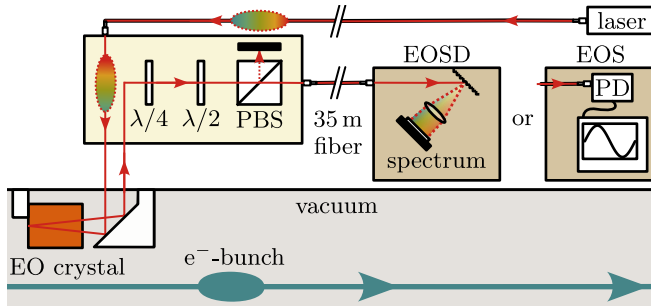


FIG. 1. Schematic of electro-optical spectral decoding (EOSD) and electro-optical sampling (EOS) at KARA. The laser is guided in a 35 m long fiber from a laboratory to the vacuum chamber of KARA, through the EO crystal, a polarizer and back to the laboratory for the analysis and data acquisition. The fiber can either be connected to a spectrometer for single-shot bunch profile measurements with EOSD, or to a photodiode (PD) for an EOS scan of the averaged Coulomb- and wakefield of the electron bunch.

amplitude modulation by sending it through a polarizing beam splitter (PBS). The $\lambda/4$ waveplate in front thereby enables compensation for the intrinsic birefringence of the crystal, while the $\lambda/2$ waveplate is used to set the working point in a near-crossed configuration [11]. In the final step, the amplitude modulated chirped laser pulse is sent on a spectrometer, consisting of a grating followed by a focusing lens and a line camera. Due to the linear chirp, the spectrum corresponds to the longitudinal profile of the laser pulse, where the Coulomb field of the electron bunch shows as a modulation of the spectrum. For relativistic particle velocities, the measured Coulomb field corresponds to the longitudinal charge density profile of the electron bunch due to the Lorentz contraction, which leads to a longitudinally compressed field [13]. For single-shot turn-by-turn measurements, the KIT-built line camera KALYPSO [14] is used to enable measurements at the KARA revolution frequency of 2.7 MHz [15]. This turn-by-turn data has been used to investigate the dynamics of the micro-bunching instability and to recreate the longitudinal phase space in a tomographic approach [12].

For electro-optical sampling (EOS) measurements, the spectrometer is replaced by a photodiode (PD) connected to a lock-in amplifier and oscilloscope. Instead of resolving single-shot laser pulses, the delay of the laser pulse is changed in small steps, while the recorded photodiode signal amplitude provides an indication of the total laser pulse intensity. The resulting plot of the photodiode signal amplitude over the laser pulse delay provides the timing of the overlap with the electron bunch, and the general structure of the wakefield.

The achievable resolution is limited by the geometric mean of the transform-limited laser pulse $\tau_{\text{trans-lim}}$ and the stretched pulse $\tau_{\text{stretched}}$ with [16]

$$\tau = \sqrt{\tau_{\text{trans-lim}} \cdot \tau_{\text{stretched}}} . \quad (1)$$

To improve the resolution beyond this limit, methods

like electro-optic spectral interferometry (EOSI) [17] and phase diversity electro-optic sampling (DEOS) [18] are under development. Since adjusting EOSD to either of these methods is possible with minor hardware changes, this investigation of an EO setup for FCC-ee focuses on the more established EOSD setup.

III. SIMULATION OF EO MEASUREMENTS UNDER FCC-EE CONDITIONS

The first step toward the development of an EO bunch profile monitor for the FCC-ee is to test an established setup under FCC-ee conditions to uncover the challenges that need to be addressed. Since no existing accelerator can replicate the beam parameters of FCC-ee, a simulation procedure for electro-optical sampling (EOS) measurements has been set up, and its results have been compared to KARA measurements to assess its accuracy.

A. Simulation procedure

The simulations are based on the Wakefield Solver of the CST Particle Suite [19], which is used to simulate the electrical field on the inside of the EO crystal using a simplified 3-dimensional model of the vacuum chamber with the crystal and its holder. The electrical field is measured using multiple virtual probe points along a line through the crystal center. Based on this simulation, the total phase retardation caused by the Pockels effect is estimated in first order by

$$\Gamma \approx \sum_i^n \frac{2\pi d_i}{\lambda} n_0^3 r_{41} E_i^{(y)}(t_i), \quad (2)$$

considering the distance d_i between the probes i and $i+1$, the central laser wavelength $\lambda \approx 1030$ nm and the vertical part of the electrical field $E_i^{(y)}$ at probe i , as well as the refractive index n_0 of the crystal and its electro-optical coefficient r_{41} [20]. This assumes a crystal orientation for maximum phase retardation. For typical EO crystal materials like GaP and ZnTe, this is the case for the Coulomb field and the laser polarization being parallel to the $[-1,1,0]$ direction of the crystal. The propagation of the laser also needs to be taken into consideration, which leads to using the probed field at the arrival time of the laser t_i at probe i . The arrival time is calculated by assuming a constant refractive index n_0 at the central laser wavelength. Due to limitations of the simulation, Eq. 2 assumes a constant field between the probes, which is an approximation for small probe spacing. The phase retardation Γ is used in the following sections as a measure to compare the expected signal strength in different scenarios.

In the KARA EO setup, the laser initially travels through the crystal in the upstream direction, opposite to the beam direction. A reflective coating on backside

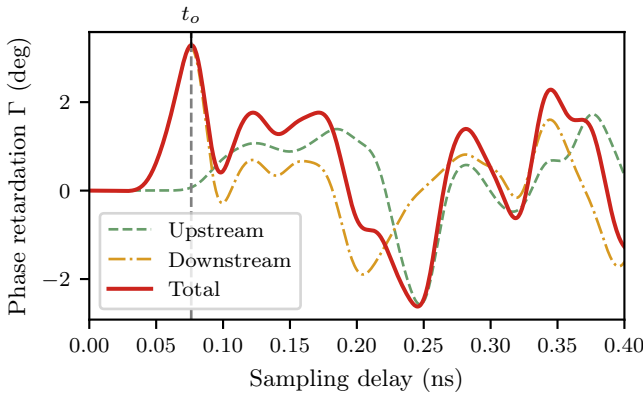


FIG. 2. Simulation of the total phase retardation Γ at KARA in red, with the upstream component in green (dashed) and downstream component in yellow (dash-dotted). t_o highlights the time of the Coulomb peak from the bunch overlapping with the laser. The later peaks of the phase retardation originate in the wakefield. Around the time of the overlap t_o , the unwanted upstream signal has a low amplitude.

of the crystal leads to a subsequent propagation in the downstream direction, in alignment with the beam direction. This two-pass process is illustrated in the schematic in Fig. 1. In the simulation, the up- and downstream laser propagation is calculated separately using Eq. 2, where the downstream signal calculation uses the same field probes as upstream, but in reverse order and at later times.

Thus, the total phase retardation of the laser is the sum of both the upstream and downstream components, as depicted in Fig. 2 for typical KARA parameters (for further details of simulation parameters, see Section III B). The shape of the first peak at t_o in the downstream signal correlates with the Coulomb field of the electron bunch and is crucial for the single-shot EOSD measurements. Although the overlap with the upstream signal can cause disturbances, the influence on the bunch profile measurement is minimal due to the relatively small amplitude of the upstream phase retardation around t_o .

After the crystal, the laser is guided through a $\lambda/4$ -waveplate at angle ϕ followed by a $\lambda/2$ -waveplate at angle θ and a PBS. The angles are defined to be 0° for a crossed configuration in which the laser is not transmitted through the PBS. The resulting detected laser intensity I_{det} and its modulation through the phase retardation Γ is described by [20]

$$I_{\text{det}}(\theta, \phi, \Gamma) = \frac{I_{\text{laser}}}{2} [1 - \cos(\Gamma - 2\phi + 4\theta) \cos^2(\phi) + \cos(\Gamma + 2\phi - 4\theta) \sin^2(\phi)], \quad (3)$$

with an initial intensity I_{laser} before the waveplates. For a typical operation, the $\lambda/4$ waveplate is set to $\phi = 0^\circ$ to only compensate for the intrinsic birefringence of the

EO crystal. With this, the equation is reduced to

$$I_{\text{det}}(\theta, \phi = 0, \Gamma) = \frac{I_{\text{laser}}}{2} [1 - \cos(\Gamma + 4\theta)], \quad (4)$$

noindent which highlights the proportionality $I_{\text{det}} \propto 1 - \cos(\Gamma)$. The working point is typically chosen to be in a near-crossed setting with $\theta \approx 5^\circ$ for two main reasons: First, in order to maximize the signal-to-noise ratio, the relative modulation of the laser

$$M = \frac{I_{\text{det}}(\theta, \phi = 0, \Gamma)}{I_{\text{det}}(\theta, \phi = 0, \Gamma = 0)} \quad (5)$$

should be as large as possible. In practice, the background from imperfect laser polarization and polarizer, as well as the noise level and response of the detector needs to be considered. Second, the correlation between the laser intensity I_{det} and the phase retardation should be kept approximately linear to simplify the interpretation of the EOSD data. Therefore, the working point should not be too close to the maximum or minimum of I_{det} . Due to the complexity of this optimization, the working point has been determined empirically for the KARA setup to be at $\theta_{\text{wp}} = 4.6^\circ$ [11].

As a result, during an EOSD measurement the modulation M is approximately linearly correlated with the Coulomb field E_y and hence corresponds to the longitudinal bunch charge density profile.

For the simulation of EOS measurements, the photodiode and the lock-in amplifier need to be considered. To emulate these devices, it is important to distinguish between two different time axes:

- The sampling delay, which is in the order of nanoseconds and describes the relative delay of the laser pulses to the KARA revolution clock. In plots of the laser modulation (e.g. Fig. 3), the time axis also describes the relative arrival time of the Coulomb and wake field.
- The measurement duration, which is in the order of minutes and describes the time that the performance of an EOS scan takes. The delay of the laser is changed stepwise, and the time for each step is typically in the order of seconds.

The laser pulses are approximated as a normalized Gaussian with length σ multiplied by the modulation M . The laser pulse length is generally greater than the bunch length, because EOSD measurements require longer pulses to resolve the bunch profile in single shot measurements. However, for EOS measurements, longer pulses limit the resolution, because the lock-in amplifier output is proportional to the integrated laser pulse intensity. As a result, the EOS scan acts similar to a moving average over the laser pulse length.

The laser pulses are measured with a photodiode, which is approximated as a low-pass filter, where the cut-off frequency is defined by its bandwidth. Therefore, this low-pass filter is applied on the sampling delay time.

The lock-in amplifier receives the photodiode signal and a reference signal with the same repetition rate as the laser, mixes both signals, and applies a low-pass filter to the output. To highlight signal changes from step to step during the scan, the time constant of this filter is set slightly shorter than the time between two EOS scan steps. However, processing every individual pulse is computationally expensive since single laser pulses are on the picosecond scale with MHz repetition rate, while the duration between EOS scan steps is in the order of seconds. To streamline the simulation process, two simplifying assumptions are applied. First, the reference signal multiplication is omitted, as the simulation does not require artificial noise filtering and focuses solely on relative modulation. Second, the low-pass filter of the lock-in amplifier is typically set to have a cut-off frequency of around 1 Hz for EOS measurements, which only shows long-term changes during the measurement duration and suppresses the signal of individual laser pulses. In summary, to emulate the data acquisition, the simulated modulation is modified by

1. multiplying with a normalized gaussian to emulate the laser pulse shape for each scan step,
2. applying a low-pass filter to the emulated laser pulses to simulate the photodiode,
3. calculating the amplitude maximum for each scan step and adding another low-pass filter over the whole scan duration to emulate the lock-in amplifier.

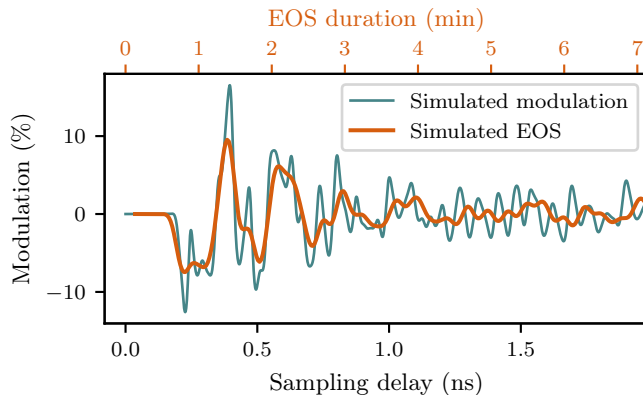


FIG. 3. Comparison of the simulated modulation M of the laser pulse (blue) and the modulation of a simulated EOS measurement (orange) including effects of the laser pulse length, the photodiode and the lock-in amplifier.

A comparison of the simulated modulation M with the simulated relative modulation after applying the low-pass filters of the photodiode and the lock-in amplifier is presented in Fig. 3, using parameters typical for EOS measurements at KARA. These parameters are a laser pulse length of $\sigma = 20.2$ ps, a photodiode bandwidth of 2 GHz

and a time constant of $\tau = 1$ s for the 4th order Butterworth low-pass filter of the lock-in assuming a time per EOS step of 1.25 s. The plot reveals that while some details are reduced after filtering, EOS remains valuable to calibrate the timing of the laser pulses and for qualitative evaluation of the Coulomb and wake-field. However, high-resolution measurements of the bunch profile need to be done with a spectrometer using EOSD.

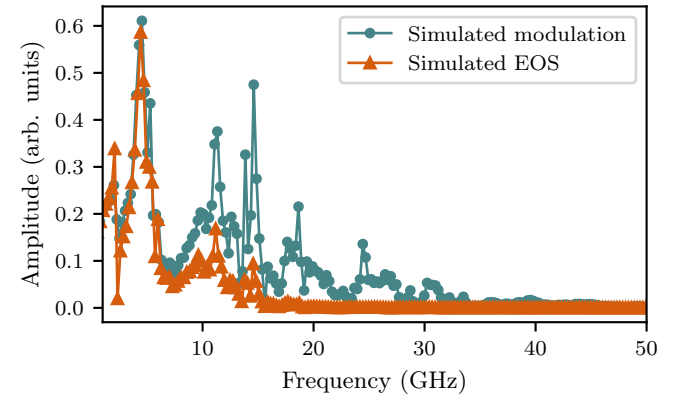


FIG. 4. Comparison of the Fourier-transformed simulated modulation M (blue) and a simulated EOS measurement (orange), corresponding to the time-domain plots in Fig. 3. It shows the low-pass filtering of the simulated data acquisition of EOS measurements in comparison to the unfiltered simulated modulation.

A look into the frequency domain is provided in Fig. 4 by a Fast Fourier Transform (FFT) of the simulated modulation and simulated EOS measurement. As expected, the low-pass filters to emulate the photodiode and lock-in amplifier lead to a suppression of higher frequencies. This is especially noticeable in the region between 8 GHz to 35 GHz, where the simulated modulation exhibits multiple amplitude peaks that are damped in the simulated EOS measurement. However, at $f \approx 4.5$ GHz both signals show a prominent peak with similar amplitude. Additional simulations suggest that this frequency originates in a resonance of the vacuum chamber, since it changes with the distance of the crystal to the electron beam and when changing the width of the vacuum chamber.

B. Comparison of simulations with KARA measurements

To assess the accuracy of the simulation procedure, an EOS measurement was performed at KARA to detect the electric field of the electron bunch and its wakefield as a reference [21]. While EOSD enables a high resolution measurement of the bunch profile with chirped laser pulses over a time span of tens of picoseconds, EOS measurements can be used to scan a longer time span in the nanosecond-scale and beyond around the electron bunch

arrival by changing the delay of the laser pulse and monitoring its intensity with a PD. Therefore, EOS is useful to find the timing t_o for the overlap of the Coulomb field of the electron bunch and the laser pulse inside the crystal. The laser pulse timing can be used for later EOSD measurements for longitudinal bunch profile measurements. However, it can also be used to sample the trailing wake-field of the electron bunch. This is an important factor for a comparison of experiment and simulation, since it depends on the geometric impedance of the EO crystal and its holder, which should be similar in both cases.

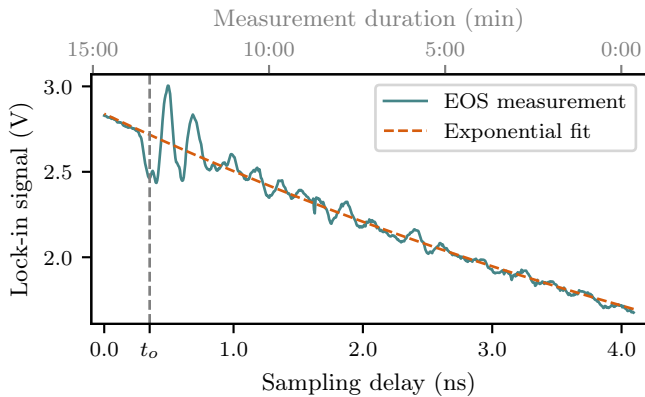


FIG. 5. KARA EOS scan with a lock-in amplifier in blue, which corresponds to the measured laser intensity with the photodiode [21]. The dashed orange line indicates an exponential fit, highlighting the general signal amplitude drift over time. The delay scan started on the right and took 15 min to complete.

For this measurement, a single bunch was injected into the storage ring, which was operated at a particle energy of 1.3 GeV. The laser repetition rate is synchronized to the RF signal of KARA (~ 500 MHz) with a phase locked loop, which enables shifting the laser delay by changing the phase of the RF signal with a vector modulator (VM). For the EOS scan, the phase was shifted in steps of $\sim 1^\circ$, resulting in a shift of the pulse delay of ~ 6 ps for a total scan range of around 4 ns. To improve the signal-to-noise ratio, the PD was connected to a lock-in amplifier using the KARA revolution frequency (~ 2.7 MHz) as a reference. Each step of the EOS scan took ~ 1.25 s, resulting in a total scan duration of ~ 15 min. To highlight the signal changes during the scan, the time constant of the lock-in was set to $\tau = 1$ s.

The resulting EOS scan is presented in Fig. 5. The measurement duration is displayed on the top axis while the delay of the laser is presented on the bottom axis. The axis of the measurement duration is reversed, since the scan was done from right to left. During the scan, the electron bunch charge decreased from approx. 0.35 nC to 0.27 nC. Additionally, the laser intensity slowly increased, likely due to a beam-induced temperature change of the crystal [21]. This changes the intrinsic birefringence of the crystal and, hence, results in a drift

of the laser polarization. To quantify this drift of the signal baseline, an exponential function was fitted to the curve. Dividing the lock-in signal by the exponential fit yields the modulation of the signal.

Figure 6 shows the measured modulation in blue compared to a simulated EOS signal in orange. The uncertainty of the measurement is estimated using the standard deviation of the unmodulated signal at the sampling delay 0 ns to 0.2 ns and the propagated uncertainty of the parameters from the exponential fit in Fig. 5. The total uncertainty is highlighted in an exemplary magnified inset plot, since the lock-in amplifier reduces the noise to a total average uncertainty of $\bar{\sigma}_{\text{total}} = 0.23\%$

The simulation follows the procedure described in the previous section, but with waveplate angles of $\phi = 7^\circ$ and $\theta = 2^\circ$. The simulation assumes constant waveplate angles, which are set to the estimated values at the time of the temporal overlap of electron bunch and laser pulse. Due to the crystal temperature change, the laser polarization changed slightly over time, which acts like a relative change of the waveplate angles over time. This effect is described in more detail in [21]. While the simulation assumes a constant bunch charge of $q(t_o) = 0.274$ nC, the bunch charge decreased during the scan. Therefore, the measured modulation is scaled with a factor of $q(t_o)/q(t)$ to compensate the modulation for the charge loss.

Compared to the measurement, the EOS simulation in Fig. 6 closely matches the main features around t_o at the temporal overlap with the Coulomb field of the electron bunch but the deviations increase for the peaks with lower amplitude of the following wakefield. Despite the simplifications made in the simulation, the amplitude of the main peaks around t_o are close to the measurement. The modulation amplitude at t_0 is $\sim 2.3\%$ smaller in the simulation, which could be caused by deviations of the laser polarization or errors in the estimation of the distance between laser pulse and electron beam, following Eq. 3 and Eq. 2. The increased amplitude of the wakefield in the measured data after around $t = 1.5$ ns is likely caused by slight changes of the laser polarization and additional impedances of the vacuum chamber. The simulation only accounts for a simplified geometry of a short section of the vacuum chamber including the crystal and its holder. Therefore, additional impedances from other hardware in and around the vacuum chamber are to be expected.

This assumption is also evident in the frequency domain in Fig. 7, which presents the FFT of the simulated and measured EOS data. While the most prominent peak at $f \approx 4.5$ GHz is in good agreement, additional peaks for example at ~ 3.7 GHz, ~ 5.1 GHz and ~ 5.9 GHz do not show in the simulation. As discussed before, these are probably due to additional impedances caused by other hardware, which is not represented in the simulation, or caused by the simplified geometry of the vacuum chamber and crystal holder in the simulation. However, only the simulation data shows a small peak at 11.2 GHz, which could also be caused by a slightly different geometry or

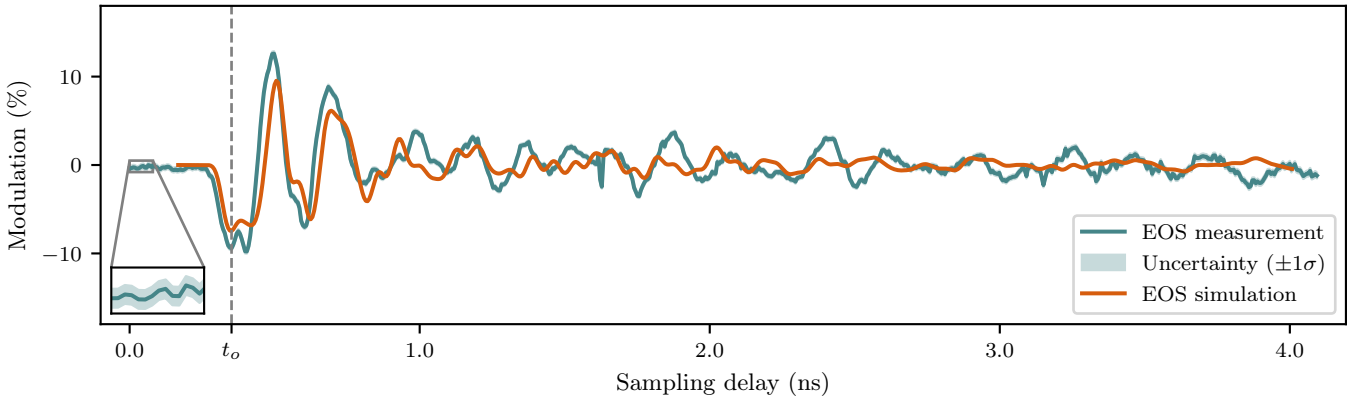


FIG. 6. Comparison of an EOS measurement (blue) at KARA with a simulation based on CST [19] (orange). The measurement includes an error band with $\pm 1\sigma$ calculated from the signal noise and the uncertainty of the baseline fit (Fig. 5). The simulation corresponds to the EOS simulation in Fig. 3.

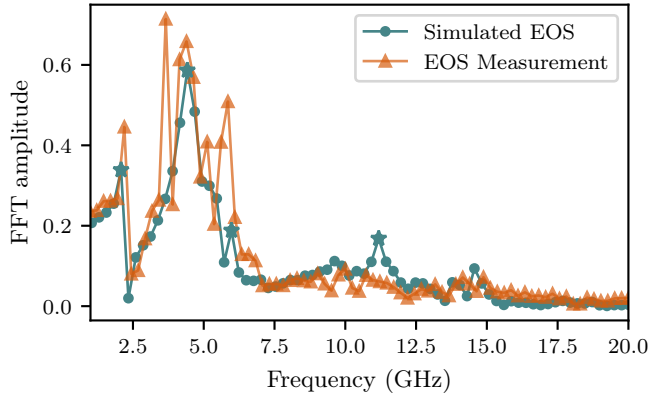


FIG. 7. FFT of EOS measurement (blue) and EOS simulation data (orange) from Fig. 6. It shows a good agreement at the most prominent peak at ~ 4.5 GHz, but it also reveals additional peaks that are only present in the measurement. The missing peaks in the simulation are likely caused by the simplified geometry of the vacuum chamber and the crystal holder.

by underestimating the low-pass filtering in the measurement, for example, by not including the cables that carry the signal from the photodiode to the lock-in amplifier.

All in all, the simulation procedure can be used to estimate the modulation amplitude of the Coulomb field and the main features of the wakefield. The closely matching wakefield enables to estimate the impedance, which is discussed later in more detail. These are important factors for the development of an EO setup for FCC-ee and can help to identify the challenges of the demanding beam parameters of the FCC-ee operation modes.

C. Simulations under FCC-ee conditions

With the goal to identify the challenges for an EO monitor, the KARA EO simulation is tested under FCC-ee

beam conditions. Since the FCC-ee study is still ongoing and the design details are under investigation, different sets of beam parameters exist for different scenarios and are frequently updated. In this contribution, the beam parameters are based on a layout including four interaction points (4 IP), which is currently the preferred option [22]. The FCC-ee beam parameters applied in the following simulations are summarized in Table I and differ for the four planned operation modes. However, the largest differences in respect of the EO setup from FCC-ee to KARA are during Z-operation due to its long bunches and during $t\bar{t}$ operation for its high bunch charge density. As a result, this contribution focuses on these two modes, since the beam parameters for W operation and ZH operation are in between those two extremes.

TABLE I. FCC-ee beam parameters for the 90.7 km circumference ring with 4 interaction points, based on [22].

Operation mode	Z	W	ZH	$t\bar{t}$
Beam energy (GeV)	45.6	80	120	183
Bunches / beam	10000	880	248	40
Bunch charge (nC)	38.73	46.41	32.57	37.82
Bunch length σ_z (mm)	15.4	8.0	6.0	2.7

Figure 8 shows the total phase retardation and its up- and downstream component for the KARA EO design under FCC-ee Z-mode conditions. The long bunches cause issues with this setup because, in contrast to the short bunches at KARA (Fig. 2), the peak of the upstream signal overlaps with the peak of the downstream signal on the first peak at t_o . While the phase retardation of the downstream signal correlates directly with the bunch profile, the correlation to the upstream signal is more complex. Since only the sum of both can be measured, the upstream signal is considered a disturbance of the measurement. Additionally, the phase retardation under FCC-ee Z mode conditions peaks at approximately 194.5° , whereas the peak at the KARA simulation has

an amplitude of approx. 3.4° . While this can lead to a higher modulation and better signal-to-noise ratio, it also causes issues. Preferably, phase retardation is kept small to achieve an approximately linear relation between the laser modulation and the Coulomb field strength of the electron bunch (see Section III A and Eq. 3). In addition, the proximity to the high intensity beam leads to high wakefield intensities and could cause potential damage to the crystal. Due to higher charge densities during W, ZH and especially $t\bar{t}$ operation, the phase retardation is expected to be even higher.

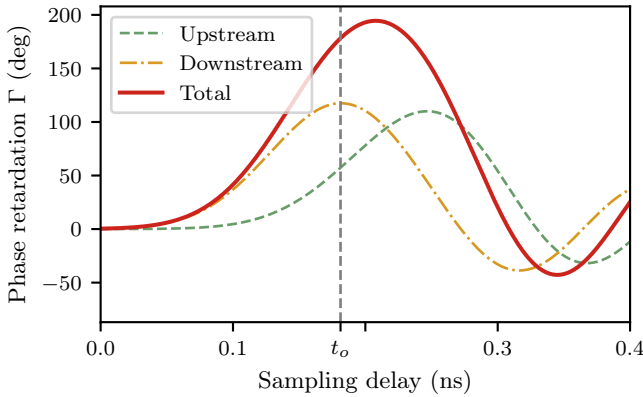


FIG. 8. Simulation for the KARA EO design under beam conditions of FCC-ee during Z-operation (see Table I). It shows the total phase retardation of the laser in red, with the upstream component in green (dashed) and downstream component in yellow (dash-dotted). At the time t_0 of the overlap of the Coulomb field with the laser, the first peak of the upstream signal overlaps with the downstream signal. This would lead to a disturbance of the bunch profile measurement and needs to be addressed in a EO setup for FCC-ee.

The mitigation of the above-mentioned issues that resulted from the simulations of the KARA EO setup under FCC-ee conditions requires a design change of the setup, which will be addressed in the following sections.

D. Concept idea for FCC-ee

A concept design for an EO monitor has been developed, which is adapted to the beam conditions of FCC-ee. Figure 9 shows an image of the 3D-model created with the CST Studio Suite [19]. It includes the planned cylindrical geometry of the FCC-ee vacuum chamber with 70 mm diameter and additional winglets in the horizontal plane [1]. To avoid the upstream signal, the laser is guided through the crystal only once in the downstream direction (single-pass), using prisms attached to its sides. The prisms are oriented to guide the laser pulses through the crystal using total internal reflection, such that no reflective coating is necessary. Due to the high charge density, the distance to the beam can be increased by positioning the crystal directly below the top of the inner FCC-ee vacuum chamber wall. Additionally, the crystal

thickness can be reduced to further decrease the phase retardation following Eq. 2. A thinner crystal also benefits the resolution of EOSD measurements, since it reduces the effects of phase mismatch between the laser and the Coulomb field of the electron bunch.

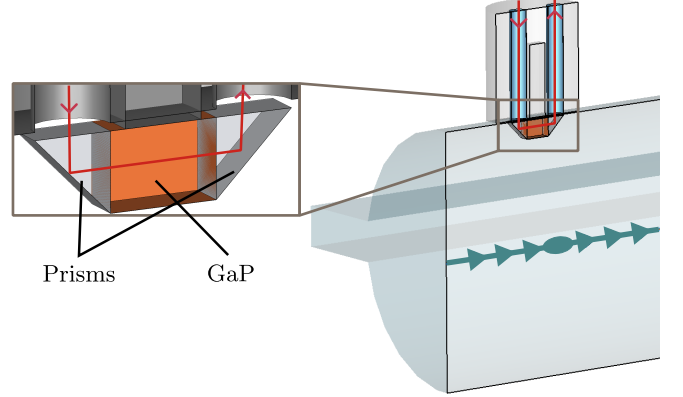


FIG. 9. Concept design of a crystal holder for FCC-ee with the GaP crystal installed between two prisms. The crystal is attached to the wall of the FCC-ee vacuum chamber, which has a diameter of 70 mm. The image shows a 3D-model created with the CST Studio Suite [23].

Figure 10 displays the phase retardation for different crystal thicknesses adapted to the FCC-ee operation modes, calculated from CST simulations. While a 7 mm thick GaP crystal is used at KARA, it could be reduced to 3 mm at FCC-ee Z operation. Despite the smaller crystal, the setup is still achieving a higher phase retardation of $\Gamma_{\max}^Z \approx 9.6^\circ$ than the KARA setup with $\Gamma_{\max}^Z \approx 3.4^\circ$. To achieve a similar amplitude for W and ZH operation, a 1 mm crystal is used in the simulation. $t\bar{t}$ operation has the largest charge density in the particle bunches and thus, the crystal thickness is reduced to 0.5 mm, which leads to a maximum phase retardation of $\Gamma_{\max}^{t\bar{t}} \approx 16.1^\circ$.

This example shows that the issue of high bunch charge density resulting in a high phase retardation can be mitigated by placing the crystal on the inner wall of the vacuum chamber. The increased distance to the particle beam reduces the phase retardation to a reasonable amplitude, which can be fine-tuned by adjusting the crystal thickness. Hence, the varying charge density across the different operation modes of FCC-ee can be accounted for by reducing the crystal size from Z mode to WW and ZH modes and from ZH to $t\bar{t}$ mode. Also, the single-pass design of the crystal holder eliminates the disturbance of the bunch profile measurement by the upstream signal.

As an additional benefit of the prism design and the larger distance of the crystal to the electron beam, the longitudinal impedance is reduced as well. The simulated real part of the longitudinal impedance is presented in Fig. 11 in comparison to the simulated impedance at KARA. While the impedance at KARA fluctuates around 100Ω with the maximum at $Z_{\max}^{\text{KARA}}(4.4 \text{ GHz}) = 340.8 \Omega$, the impedance at FCC-ee is around the 1Ω mark

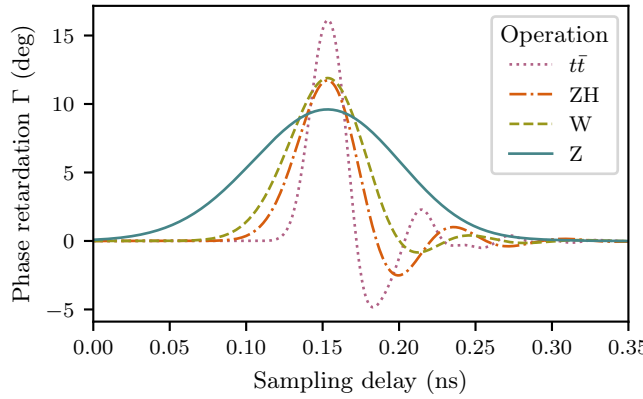


FIG. 10. Comparison of the phase retardation Γ for different FCC-ee operation modes, using varying crystal thicknesses to achieve comparable amplitudes. Z (blue, solid) operation is simulated with a 3 mm crystal thickness, W (green, dashed) with 1 mm, ZH (orange, dash-dotted) with 1 mm and $t\bar{t}$ (purple, dotted) with 0.5 mm.

with the maximum at $Z_{\max}^{\text{FCC-ee}}(9.3 \text{ GHz}) = 5.4 \Omega$. The reduced impedance of the FCC-ee concept design is beneficial to reduce impact on the beam dynamics as well as reducing the heat load on the crystal and its holder to minimize a signal drift.

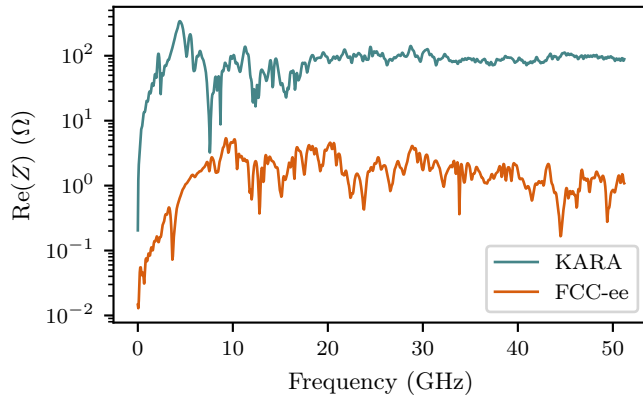


FIG. 11. Comparison of the simulated longitudinal impedance $\text{Re}(Z)$ at KARA (blue) with a 7 mm thick GaP crystal and the concept for FCC-ee (orange) with a 3 mm thick crystal. It shows, that the impedance of the FCC-ee concepts is generally around 2 orders of magnitude smaller.

In summary, the simulations show promising results for the concept design for FCC-ee. By attaching the crystal to the wall of the vacuum chamber, the distance to the beam is large enough to decrease the impedance by an order of magnitude, while still maintaining a sufficient phase retardation of the laser pulse. The crystal thickness can be used to adjust the amplitude to the different operation modes and optimize the resolution. Due to the prisms at the front and back of the crystal, the laser propagates through the crystal only in downstream direction and keeps the setup compact.

IV. PROTOTYPE TEST AT CLEAR

In order to conduct a proof-of-principle experiment, a prototype for the crystal holder with prisms has been built and tested at the CERN Linear Electron Accelerator for Research (CLEAR) in Geneva, Switzerland [24]. CLEAR is a linear accelerator and user facility with an in-air test stand at its end. This is the ideal test bed for a proof-of-principle experiment of the FCC-ee EO prototype, as the measurement setup does not need to be vacuum tight and the crystal and other parts are easily accessible for adjustments. The CLEAR electron beam is created on a CsTe photo-cathode pulsed by an UV (converted from IR) laser and accelerated by linacs to up to 220 MeV. Each electron pulse is made of 1 to 150 bunches with a bunch separation of 666 ps. The pulse repetition rate ranges from 0.833 to 10 Hz. With bunch charges of up to 1 nC at a bunch length of around 7 ps, CLEAR provides suitable parameters for a first test of the EO prototype.

A. Prototype design

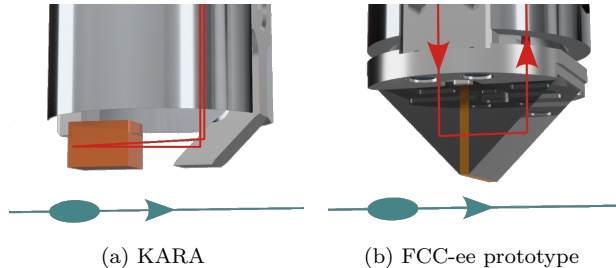


FIG. 12. Rendered 3D models of (a) the crystal holder at KARA and (b) FCC-ee prototype for proof-of-principle experiments at CLEAR (CERN). The laser path is indicated with a red line and the orbit of the particle bunches in blue, while the EO crystal is highlighted with an orange color. CAD model by S. Schott; rendered by the authors.

The prototype design is based on the crystal holder at KARA, which is presented as a rendered image of a 3D-model in Fig. 12a. At KARA, the crystal is glued to a holder on one side at the end of a metal arm. On the opposite side, a mirror is attached to guide the laser through the crystal. The crystal has an anti-reflective coating facing the mirror and a reflective coating on its backside. As a result, the laser follows down the metal arm onto the mirror, which guides the laser through the crystal until it hits the reflective backside. This sends the laser back to the mirror and finally back up through the metal arm to a metal enclosure, which contains the polarizer setup depicted in Fig. 1. After the polarizer, the laser is coupled in a single-mode fiber to eventually end at a PD. The crystal used at KARA is a GaP crystal with a size of 5 mm \times 5 mm \times 7 mm, which is used in

combination with a Ytterbium fiber laser system with a central wavelength around 1030 nm.

The prototype to evaluate the FCC-ee concept has a modified crystal holder, which enables keeping the setup similar to the KARA version. It serves as a proof-of-principle for the concept design. A rendered image is presented in Fig. 12b, where the EO crystal is installed between two prisms. Since a metal mirror upstream of the crystal would shield it from the electric field of the electron bunch, fused silica prisms are used instead. The prisms are glued to a metal plate at the top, which has holes to let the laser pass through. Unlike the KARA setup, the laser is only propagating downstream through the crystal, avoiding the upstream signal. A 10 mm \times 10 mm \times 2 mm ZnTe crystal is used for the EO crystal at CLEAR to provide better phase matching with the available 780 nm laser [25].

B. Experimental setup

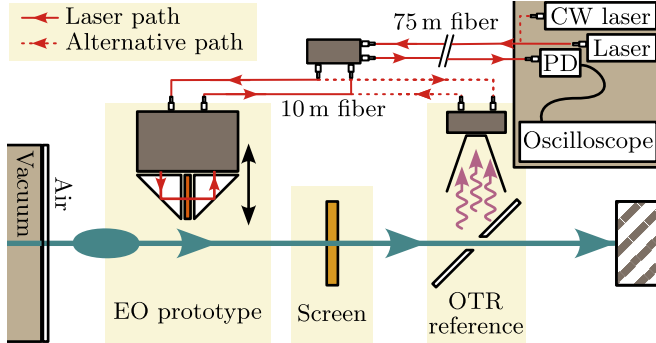


FIG. 13. Experimental setup at CLEAR to test the EO prototype for FCC-ee. The laser path is highlighted as a red line, where 75 m of optical fiber transport the laser light from a pulsed or CW laser in a laboratory to a fiber optic patch panel at the CLEAR accelerator and back. From the patch panel, a 10 m fiber can be connected to the EO prototype or alternatively to an EO modulator to detect the OTR radiation as a timing reference.

Figure 13 presents a schematic which shows a top-down view of the in-air experimental area at CLEAR. The EO prototype is installed horizontally on a linear stage, which enables adjusting the distance to the electron beam. A visible alignment laser along the ideal electron beam path has been used to calibrate the distance between beam center and crystal during the installation. An additional screen enables alignment of the electron beam to its center and estimating its horizontal and vertical size. Additionally, the distance of the crystal can be monitored by looking for an edge on the screen image, where the crystal starts blocking electrons from hitting the screen.

A 780 nm pulsed laser with 80 MHz repetition rate is delivered from a nearby laboratory through a 75 m long

polarization-maintaining fiber to a patch panel in the experimental area. There, an additional 10 m fiber can be connected to either the EO prototype or an EO modulator to measure the OTR, which is explained in more detail in the next paragraph. At the EO prototype, the laser is propagating to the crystal in free-space within a metal enclosure and afterward to motorized $\lambda/4$ and $\lambda/2$ waveplates followed by a PBS. Then, the laser is coupled back into a 10 m + 75 m single mode fiber and sent back to the laboratory. For EOS measurements, the fiber is connected to a PD with a bandwidth of 12 GHz, which is read out by an oscilloscope with 10 GHz bandwidth. However, in order to reduce high frequency noise from nearby klystrons, the oscilloscope has been digitally limited to a bandwidth of 3 GHz.

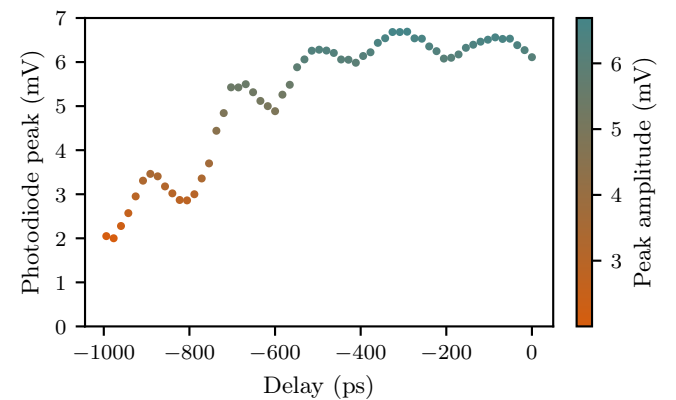


FIG. 14. Peak amplitude on the photodiode during a 1 ns scan with the delay stage. The laser alignment was optimized for the zero-position and the amplitude decreases for larger delays due to the movement of the delay stage. Each data point shows the average amplitude over 100 shots. The standard error of the mean is also included, but very small. The delay is calculated based on the step size of the linear stage. This color gradient is used in the following plots to indicate the peak amplitude.

The laser pulse needs to be overlapped in the crystal with the transient electrical field of the electron bunch. One of the major challenges was achieving precise timing, as the laser delay could only be adjusted by up to 1 ns using a delay stage. To get a rough estimation of the timing, a second screen was set up in the beam path to produce OTR. The OTR was collected with a horn antenna and measured with an electro-optical modulator, similar to the setup described in [6]. Since the setup leads to a strong laser modulation, it could be operated with a continuous wave laser, eliminating the need to synchronize the laser pulses with the electron beam. The PD showed the continuous signal of the laser with a peak occurring every time OTR was generated by the electron bunch, which was used as a trigger for the oscilloscope. Since it was using the same fiber optics as for the FCC-ee EO prototype, the timing of this peak could be used as a reference for the FCC-ee EO prototype with the pulsed laser.

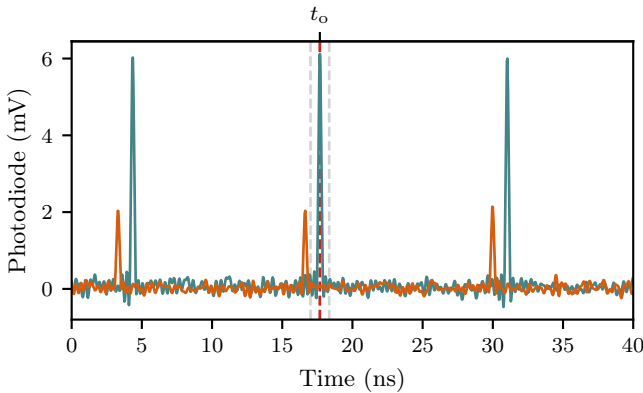


FIG. 15. Oscilloscope trace of the photodiode signal containing the peaks of three laser pulses. The blue curve shows the signal at the beginning of the delay stage and the orange curve after a delay scan of 1 ns. The red dashed vertical line describes the estimated position t_o for a temporal overlap of the laser pulse with the electron bunch. The neighboring two gray lines show the relative position of the other two bunches in the train.

Changing the delay of the laser pulses by moving the delay stage led to slight misalignment of the laser. This led to changes in laser power at the experiment due to changes in the coupling efficiency when coupling into the fiber leading from the laser laboratory to the experiment at CLEAR. Figure 14 shows the measured laser amplitude at the PD when changing the delay of the laser pulse by 1 ns. The laser alignment was optimized for the starting point of the delay scan, but during the scan, the amplitude dropped due to the laser misalignment at the fiber coupler caused by the movement of the delay stage.

Figure 15 shows the PD signal of three laser pulses. The blue curve shows the signal at the start of a delay scan, while the orange curve shows the signal with lower amplitude at the end after a delay shift of 1 ns. Based on the timing of the OTR reference measurement and the estimated optical laser path length difference of the EO prototype, the timing for the temporal overlap with the electron bunch of the EO prototype was estimated and is marked as t_o .

During the measurements, an additional bunch before and after the reference bunch were produced, to increase the chances of finding the overlap within range of the delay stage. The expected arrival time of these bunches is presented as gray dashed lines next to the original bunch at t_o . As a result, CLEAR was producing bunch trains at 10 Hz, with each train consisting of three bunches with a spacing of approx. 666 ps and a bunch charge of approx. 1 nC per bunch.

To calculate the modulation, the PD signal amplitude needs to be compared to an unmodulated signal. Therefore, three laser pulses were monitored on the oscilloscope, but only the second one was expected to overlap with electron bunches and the other two were used as unmodulated reference.

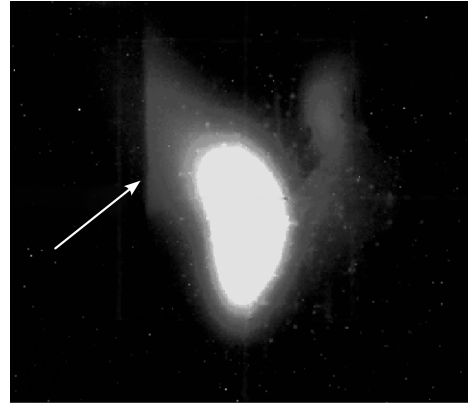


FIG. 16. Screenshot of a beam screen image showing the transverse shape of the electron beam. A portion of the electron beam is obstructed by the EO crystal and prisms, resulting in a subtle shadow on the left side of the image, which is highlighted by an arrow. In this case, the crystal was moved to an approximate distance of $d = 2$ mm to the beam center. The colors have been adjusted and transformed to grayscale to improve the visibility of the shadow, while the beam center is overexposed.

C. EOS measurements

To achieve maximum modulation amplitude, the crystal was positioned approximately 2 mm from the electron beam's center. At this distance, the crystal started blocking some of the outer electrons, which is presented in the screenshot of a beam screen image in Fig. 16. The colors have been shifted and transformed to grayscale for better visibility and a white arrow was added to highlight the crystal shadow.

For the first test, the working point was set to the angle of the $\lambda/4$ waveplate to $\phi \approx 0^\circ$ and of the $\lambda/2$ waveplate to $\theta \approx 14.2^\circ$. θ is chosen to have a greater value than at KARA to increase the laser signal amplitude, because, especially toward a laser delay of 1 ns, the signal-to-noise ratio would otherwise be too low.

The EOS scan was done by scanning the delay of the laser pulse to up to 1 ns, while recording 100 measurements per step. As described previously in Fig. 15, the oscilloscope monitors three laser pulses simultaneously, but the modulation by the electron bunch is expected to only occur at the second bunch. The first and third laser pulse are used as a reference pulse without modulation. Thus, the circular markers in Fig. 17a show the modulation as a division of the amplitude of the second laser pulse by the third laser pulse, while the triangular markers show the division of the second and the first laser pulse. Every data point and error bar is calculated based on the average of 100 shots and its standard error of the mean, which increases during the scan, because the laser amplitude decreases (see Fig. 14).

The plot shows positive peaks with around 5 % modulation at t_{o1} and t_{o2} , which are followed by a ringing. These positive peaks are 666 ps apart, which fits well to

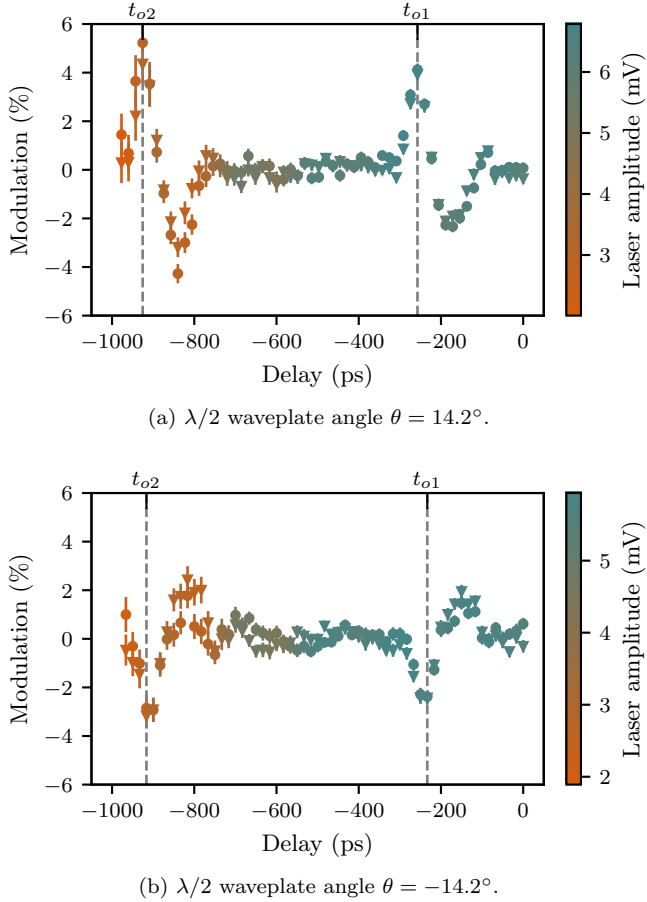


FIG. 17. Modulation of laser pulse 2 caused by 2 bunches with a spacing of 666 ps. The circular markers show the modulation of pulse 2 compared to pulse 3, while the triangular markers show pulse 2 compared to pulse 1. The error bars show the standard error of the mean and the color gradient indicates the amplitude of the photodiode signal (see Fig. 14).

the expected bunch spacing within a bunch train and the ringing could originate in the wakefield. The laser pulse length was estimated to be a multiple of the electron bunch length of around $\sigma_{e^-} = 7.5$ ps. Together with the limited bandwidth of the PD and oscilloscope, the EOS scan was expected to act similar to a moving average over the actual wakefield and, therefore, losing the high frequency details (see also Section III B).

This experiment run was followed by another EOS scan, but with the $\lambda/2$ waveplate rotated in the other direction to approx. $\theta \approx -14.2^\circ$ to test, if the EOS measurement behaves as expected. If the previously observed modulation is the EOS signal of an electron bunch, it should satisfy Eqs. 3 and 4 and lead to the modulation having the opposite sign. The result is plotted in Fig. 17b, which shows the expected result of two negative peaks at t_{o1} and t_{o2} followed by a ringing. However, the modulation amplitude dropped to around 2.5 %, the cause of which is not yet fully understood. The second measurement was performed a few hours after the first

and due to machine operation issues, the machine parameters needed to be re-adjusted to optimize the bunch charge transport through CLEAR. The modulation difference is likely caused by a slightly lower bunch charge compared to the previous measurement and a potentially high uncertainty on the angle of the $\lambda/2$ waveplate.

In summary, these measurements of the first EO monitor prototype for FCC-ee demonstrate the viability of using prisms attached to the crystal. This innovative design enables bunch profile measurements for both long and short bunches while maintaining a compact geometry, marking a substantial step forward in the development of a longitudinal bunch diagnostic that meets the requirements for the various operation modes of FCC-ee.

V. SUMMARY

The development of advanced longitudinal beam diagnostics is essential for the future electron-positron collider to monitor bunch length and bunch profile with high precision. This study demonstrates the feasibility of an electro-optical (EO) setup, which specifically addresses the challenge of being able to measure the profile of long bunches as well as short bunches with high bunch charge. To assess the specific challenges at the future circular electron-positron collider (FCC-ee), a simulation procedure has been developed based on the EO setup at the Karlsruhe Research Accelerator (KARA). The setup at KARA is optimized for low bunch charges and short bunches and has a two-pass design, where the laser travels upstream through the crystal, is reflected at the backside and subsequently travels downstream parallel to the electron bunch. This design limits its use for longer bunches, because the upstream signal starts to overlap with the bunch profile in the downstream signal, making it difficult to extract the bunch profile in the final measurement. Therefore, it is unsuitable for measuring the long, high-charge bunches during Z-operation at FCC-ee. Thus, an innovative single-pass design of the crystal holder has been developed, which uses two prisms attached to the sides of the crystal to guide the laser through the crystal only once. The novel design enables measurements of long and short bunches while still keeping the setup compact with substantially reduced impedance. A corresponding prototype has been built for initial testing at the in-air test area at the CERN Linear Electron Accelerator for Research (CLEAR).

The prototype was successfully tested with electro-optical sampling (EOS) measurements at the in-air test area at CLEAR, yielding a clear scan of two electron bunches and their wakefield, thereby validating the concept's functionality. This proof-of-principle marks a milestone toward realizing a longitudinal bunch diagnostic, which meets the requirements for FCC-ee. Future work will focus on optimizing the design for installation at FCC-ee and electro-optical spectral decoding (EOSD) tests along with technical details about the laser and

crystal material to enhance the resolution of bunch profile measurements. In addition, measurements during multi-bunch operation at FCC-ee provide challenges which need to be investigated, especially considering an increased heat load and exposure to radiation.

Note added. While this manuscript was under preparation, one of the coauthors, Stefano Mazzoni, sadly passed away.

VI. ACKNOWLEDGEMENTS

The authors thank Steffen Schott for assistance with the CAD design of the experimental setup. This project

has received funding from the European Union's Horizon 2020 research and innovation programme under grant agreement No 951754 (FCCIS) and No 101057511 (EURO-LABS). M. R. acknowledge funding from the Bumdesministerium für Bildung und Forschung (BMBF) under contract number 05K22VKB.

-
- [1] A. Abada, M. Abbrescia, S. S. AbdusSalam, I. Abdulkhanov, J. Abelleira Fernandez, A. Abramov, M. Aburaia, A. O. Acar, P. R. Adzic, P. Agrawal, J. A. Aguilar-Saavedra, J. J. Aguilera-Verdugo, M. Aiba, I. Aichinger, G. Aielli, A. Akay, A. Akhundov, H. Ak-sakal, J. L. Albacete, S. Albergo, *et al.*, The European Physical Journal Special Topics **228**, 261 (2019).
- [2] Home | Future Circular Collider, <https://fccis.web.cern.ch/> (2024).
- [3] M. Benedikt, W. Bartmann, J.-P. Burnet, C. Carli, A. Chance, P. Craievich, M. Giovannozzi, C. Grojean, J. Gutleber, K. Hanke, A. Henriques, P. Janot, C. Lourenco, M. Mangano, T. Otto, J. H. Poole, S. Rajagopalan, T. Raubenheimer, E. Todesco, L. Ulrici, T. P. Watson, G. Wilkinson, F. Zimmermann, and B. Auchmann, *Future Circular Collider Feasibility Study Report Volume 1: Physics and Experiments*, Tech. Rep. CERN-FCC-PHYS-2025-0002 (CERN, 2025).
- [4] M. Benedikt, W. Bartmann, J.-P. Burnet, C. Carli, A. Chance, P. Craievich, M. Giovannozzi, C. Grojean, J. Gutleber, K. Hanke, A. Henriques, P. Janot, C. Lourenco, M. Mangano, T. Otto, J. H. Poole, S. Rajagopalan, T. Raubenheimer, E. Todesco, L. Ulrici, T. P. Watson, G. Wilkinson, F. Zimmermann, and B. Auchmann, *Future Circular Collider Feasibility Study Report Volume 2: Accelerators, technical infrastructure and safety*, Tech. Rep. CERN-FCC-ACC-2025-0004 (CERN, 2025).
- [5] J. Keintzel, A. Abramov, M. Benedikt, M. Hofer, P. Hunchak, K. Oide, T. Raubenheimer, R. Tomás García, and F. Zimmermann, Proceedings of the 65th ICFA Advanced Beam Dynamics Workshop on High Luminosity Circular e+e- Colliders **eeFACT2022**, 9 pages, 0.585 MB (2022), artwork Size: 9 pages, 0.585 MB ISBN: 9783954502363 Medium: PDF Publisher: JACoW Publishing, Geneva, Switzerland.
- [6] A. Schlögelhofer, *Non-Invasive Beam Diagnostic Development for FCC Using Cherenkov Diffraction Radiation in Dielectric Materials*, Thesis, Technische Universität Wien (2024).
- [7] I. Wilke, A. M. MacLeod, W. A. Gillespie, G. Berden, G. M. H. Knippels, and A. F. G. van der Meer, Physical Review Letters **88**, 124801 (2002).
- [8] B. Steffen, V. Arsov, G. Berden, W. A. Gillespie, S. P. Jamison, A. M. MacLeod, A. F. G. van der Meer, P. J. Phillips, H. Schlarb, B. Schmidt, and P. Schmüser, Physical Review Special Topics - Accelerators and Beams **12**, 032802 (2009).
- [9] B. Steffen, C. Gerth, M. Caselle, M. Felber, T. Kozak, D. R. Makowski, U. Mavrić, A. Mielczarek, P. Peier, K. Przygoda, and L. Rota, Review of Scientific Instruments **91**, 045123 (2020).
- [10] N. Hiller and E. Huttel, in *IPAC 11* (2011) p. 3.
- [11] N. Hiller, *Electro-Optical Bunch Length Measurements at the ANKA Storage Ring*, Ph.D. thesis, Karlsruhe (2013).
- [12] S. Funkner, G. Niehues, M. J. Nasse, E. Bründermann, M. Caselle, B. Kehrer, L. Rota, P. Schönfeldt, M. Schuh, B. Steffen, J. L. Steinmann, M. Weber, and A.-S. Müller, Scientific Reports **13**, 1 (2023).
- [13] M. Ota, K. Kan, S. Komada, Y. Wang, V. C. Agulho, V. K. Mag-usara, Y. Arikawa, M. R. Asakawa, Y. Sakawa, T. Matsui, and M. Nakajima, Nature Physics **18**, 1436 (2022).
- [14] L. Rota, M. Caselle, E. Bründermann, S. Funkner, Ch. Gerth, B. Kehrer, A. Mielczarek, D. Makowski, A. Mozzanica, A. S. Müller, M. J. Nasse, G. Niehues, M. Patil, B. Schmitt, P. Schönfeldt, B. Steffen, and M. Weber, Nuclear Instruments and Methods in Physics Research Section A: Accelerators, Spectrometers, Detectors and Associated Equipment Frontiers Detectors for Frontier Physics: 14th Pisa Meeting on Advanced Detectors, **936**, 10 (2019).
- [15] S. Funkner, E. Blomley, E. Bründermann, M. Caselle, N. Hiller, M. J. Nasse, G. Niehues, L. Rota, P. Schönfeldt, S. Walther, M. Weber, and A.-S. Müller, Physical Review Accelerators and Beams **22**, 022801 (2019).
- [16] F. G. Sun, Z. Jiang, and X.-C. Zhang, Applied Physics Letters **73**, 2233 (1998).
- [17] Walsh, David, Pace, Thomas, Snedden, Edward, and Okell William, in *14th International Particle Accelerator Conference* (Venice, Italy, 2023) pp. 4855–4858 pages.
- [18] E. Roussel, C. Szwaj, C. Evain, B. Steffen, C. Gerth, B. Jalali, and S. Bielawski, Light: Science & Applications **11**, 14 (2022).
- [19] Dassault Systems, CST Studio Suite (2021).
- [20] B. R. Steffen, *Electro-Optic Methods for Longitudinal Bunch Diagnostics at FLASH*, Ph.D. thesis, Universität

- Hamburg (2007).
- [21] M. Reissig, A. Mochihashi, Mueller, Anke-Susanne, Haerer, Bastian, Bruendermann, Erik, Niehues, Gundrun, Steinmann, Johannes, Patil, Meghana, Ruprecht, Robert, and Funkner, Stefan, in *Proc. IPAC'24* (JACoW Publishing, 2024) pp. 2354–2357 pages, 0.52 MB.
- [22] F. Zimmermann and M. Benedikt, in *65th ICFA Advanced Beam Dynamics Workshop on High Luminosity Circular E+e- Colliders (eeFACT'22), Frascati, Italy, 12-16 September 2022* (JACoW Publishing, Geneva, Switzerland, 2022) pp. 7–13.
- [23] M. Reißig, M. Brosi, E. Bründermann, S. Funkner, B. Häger, A.-S. Müller, G. Niehues, M. Patil, R. Ruprecht, and C. Widmann, in *13th International Particle Accelerator Conference (IPAC'22), Bangkok, Thailand, 12-17 June 2022* (JACoW Publishing, Geneva, Switzerland, 2022) pp. 296–299.
- [24] D. Gamba, R. Corsini, S. Curt, S. Doeberl, W. Farabolini, G. Mcmonagle, P. Skowronski, F. Tecker, S. Zeeshan, E. Adli, C. Lindstrøm, A. Ross, and L. Wroe, Nuclear Instruments and Methods in Physics Research Section A: Accelerators, Spectrometers, Detectors and Associated Equipment **909**, 480 (2018).
- [25] B. Wu, L. Cao, Q. Fu, P. Tan, and Y. Xiong, Proceedings of the 5th Int. Particle Accelerator Conf. **IPAC2014**, Germany (2014).